A Generic Power Compensation Control for Grid Forming Virtual Synchronous Generator With Damping Correction Loop

Yang, Yaqian; Li, Chang; Cheng, Long; Gao, Xingle; Xu, Jiazhu; Blaabjerg, Frede

Published in:
IEEE Transactions on Industrial Electronics

DOI (link to publication from Publisher):
10.1109/TIE.2023.3342332

Publication date:
2024

Document Version
Accepted author manuscript, peer reviewed version

A Generic Power Compensation Control for Grid Forming Virtual Synchronous Generator with Damping Correction Loop

Yaqian Yang, Chang Li, Long Cheng, Xingle Gao, Jiazhu Xu, *Member, IEEE*
and Frede Blaabjerg, *Fellow*, *IEEE*

***Abstract*—Insufficient damping and inertia is the one of the most tough challenges in the grid-connected power system with high penetration of renewable energy resources. Damping correction loop of virtual synchronous generator (VSG) connected to weak damping and high R/X ratio condition is introduced to solve the issues. Firstly, the scheme of the proposed control is implemented in various system operating conditions, and the small-signal model of the proposed control is established. Subsequently, the influence of the damping correction loop on small-signal stability is demonstrated by Bode diagram analysis, and the interaction between reshaped VSG control and power compensation capacity is clarified in three aspects of damping, inertia and synchronization. Furthermore, the optimal design of additional damping and inertia support is provided to suppress the sub-synchronous frequency fluctuation of the system, the proposed control method can be easily implemented by directly inserting it into active power control loop of VSG. Finally, the efficiency of the damping correction loop is verified by experiments, the results indicate that 70% reduction of maximum frequency deviation with the proposed control under 20% active power reference step.**

***Index Terms*—Power compensation capacity, virtual synchronous generator, damping correction loop, frequency fluctuation.**

I. INTRODUCTION

THE fossil fuel energy resources are gradually getting exhausted, which stimulates the rapid development of renewable energy sources (RESs). Inevitably, power electronics converters are required for the integration of RESs, which drives the modern power system more power electronics-dominated [1]. Power electronics converters bring flexibility and controllability for power electronics-dominated power systems (PEDPS). Unfortunately, it also brings several disadvantages, such as significantly declined level of inertia and damping, which induces several stability issues, e.g., frequency oscillation and active power oscillation [2]. To suppress the fluctuation of frequency and active power of PEDPS caused by low inertia and damping, the virtual synchronous generator (VSG), which emulates the dynamic property of traditional synchronous generator, was proposed to provide sufficient support of inertia and damping. Unfortunately, VSG inevitably interacts with the power network, where new stability issues will arise [3]-[4]. Therefore, it is significant to explore the stability mechanism hidden in grid-forming VSG (GF-VSG) attached to power network.

The researches on topic of GF-VSG are mainly focused on two aspects, i.e., modeling approach and mechanism analysis of stability. When discussing the stability of GF-VSG attached to power network, three mainstream approaches are adopted, i.e., impedance modeling [3]-[4], state-space model with eigenvalue analysis [5]-[11], and magnitude-phase-motion equation (MPME) [11]-[13], and etc. Every method has its advantage and disadvantage. In [3], impedance model considering VSG control was proposed in voltage source converter high voltage direct current system to clarify the mechanism of frequency oscillation. In addition, sequence impedance model was put forward to develop comparison analysis of VSG and grid-connected inverters [4]. State-space model was developed for frequency stability analysis in VSG in different scenarios, including mechanism of oscillation in renewable energy generator [5], damping method of low frequency oscillation in VSG [6], the application of grid-following distributed virtual inertia [7], and small signal modeling of grid-tied system [8], [9]. In addition, the impact of virtual synchronous machine on low-frequency oscillation (LFO) of power systems was also investigated by state-space model [10]-[11], where the characteristics of the LFO modes and the dominant states have been comprehensively in all-VSM grid. Besides of this, a damping torque model was proposed to study the Inner Controls Effects of VSG-Controlled Converter under low control bandwidths and weak grid conditions [12]. The impact of VSG on stability of power system was seen from

Yaqian Yang and Long Cheng are with the School of Engineering, Anhui Agricultural University, Hefei 230036, China (e-mail: yaqianyang@ahau.edu.cn; cl@ahau.edu.cn).

Chang Li is with the School of Electrical and Automation Engineering in Hefei University of Technology, Hefei 230009, China (e-mail: changli@hnu.edu.cn) (Corresponding author)

Jiazhu Xu is with the College of Electrical and Information Engineering, Hunan University, Changsha 410082, China (e-mail: xjz@hnu.edu.cn).

Xingle Gao is with Economic Research Institute of State Grid Hebei Electric Power Co., Ltd. Shijiazhuang, China (e-mail: Xinglegao@hnu.edu.cn).

Frede Blaabjerg is with the Institute of Energy Technology, Aalborg University,9220 Aalborg, Denmark (e-mail: fbl@et.aau.dk).

another perspective that the frequency stability assessment of GF-VSG attached to weak AC network was investigated by using MPME model [13]. The above literatures reported the study on the impact of VSG on power systems stability from various perspectives.

From perspectives of different stability phenomena of VSG, the research can be classified into rate of change of frequency (RoCoF) / frequency nadir (FN) issues [9], [14]-[15], [25]-[26], periodic oscillation [9]-[10], [14], [17], [19]-[23], [29] and its suppression [5], [7], [16], [19]-[21], [23]-[24], [26]-[27]. In fact, the periodic oscillation can be regarded as the periodic variation of RoCoF and FN as both RoCoF and FN are gets higher or lower depending on divergent oscillation or convergent oscillation. For an example, a VSG control strategy was proposed for battery/ultracapacitor hybrid energy storage system to implement power management of grid-connected system [15]. The RoCoF declined and FN was improved by the proposed VSG control. In addition, the require energy of realization of virtual inertia support was discussed with considering the multi-timescale stability in renewable energy generation system [9], where the interaction between DC voltage and AC frequency was analyzed. The new framework, which relates RoCoF with FN, was proposed for wideband stability evaluation in renewable energy generator [22]. Specifically, the mechanism of both oscillation-stability and synchronous-stability was clarified in details. Furthermore, the operation region of the VSG was discussed by changing the virtual inertia factor and virtual damping constant [14].

Besides of RoCoF/FN issues, the wideband oscillation issues will also impose bad effect on stable and secure operation of PEDPS. The mechanism of active power allocation as well as power oscillation in paralleled VSGs was clarified with different virtual inertia factors [2]. In [10]and [11], the impact of VSG on the dynamic stability of the power system was investigated comprehensively. Also, the grid-synchronization interaction mechanism between VSG and weak power network was studied by means of the built small signal model [17]. However, the above references have not addressed the issue of equivalence calculation of inertia and damping, as will be discussed herein.

To overcome the stability issues caused by low inertia and weak damping, several control measures have been proposed to improve stability of the system [13], [15], [18], [20]-[22], [24]-[26], [28]. For an example, the utilization of potential inertia stored in battery/ultracapacitor hybrid energy storage system was proposed to leave RoCoF slower and lessen frequency deviation [15]. Besides of this, a virtual resistor or virtual inductor or virtual impedance is usually employed to dampen synchronous frequency resonance (SFR), considering the dynamics of the grid equivalent impedance, the mechanism of SFR and the nonminimum phase effect are revealed [18]-[21], [28]. In [26], a self-adaptive inertia and damping combination control of VSG was proposed to support frequency stability. Even though power system stability was improved by VSG control strategy [22], [24]-[25], the grid-integration of VSG may trigger new arisen stability issues if the parameters are inappropriate. Therefore, a damping correction loop control is proposed in this research to improve the damping performance and thus enhance stability of the GF-VSG system.

To this end, the stability mechanism analysis as well as mitigation measures have not been discussed comprehensively in perspectives of support of inertia, damping and synchronization, which will be filled up in this research. The main ***contributions*** of this research are summarized as follows:

1) A damping correction loop is proposed to improve the damping and stability of VSG with high ratio of R/X. Besides, the effectiveness of the proposed control strategy is clarified by the built small signal model with frequency-domain analysis. Phase margin increment (PMI) of the system is always approximately 31 deg in the process of R_g/X_g growth.

2) The interaction between the reshaped VSG control and power compensation capacity is clarified in three aspects, i.e., damping, inertia, and synchronization of the system. The proposed control strategy significantly improves both additional inertia and damping with wide adjustment range.

3) The optimal design of additional damping and inertia support is provided to suppress the sub-synchronous frequency fluctuation of the system with satisfying stability margin as well as good dynamic property. It takes shorter time than we expect to converge to a steady state when $T_P(s)=(0.8833s+1)/(6s+1)$ was employed. The power waveforms, frequency and grid-connected current respond to their reference change smoothly without any overshoot under the active power disturbance.

The remainders of this paper are organized as follows. In the next Section, the operation principle of damping correction loop is introduced for GF-VSG system. In Section III, the stability analysis of VSG with damping correction loop is studied comprehensively. Specifically, the inertia and damping support capability under various operation conditions are discussed. Besides, the impact of damping and synchronizing effect is analyzed, and the oriented-design of control parameters is given. Section IV presents the experiments validation to verify the effectiveness of the proposed methodology. Section V draws the conclusion.

II. GF-VSG System Description with Damping Correction Loop

A. System Schematic of GF-VSG

The grid-connected distributed power system based on virtual synchronous generator control consists of different components, which include grid-forming inverter, L filter, power grid and VSG control. The VSG control is introduced to provide virtual inertia and virtual damping for the distributed power system with high penetration of RESs. However, the VSG connected to distributed power system through a large R/X may result a power oscillation, owning to the interaction between active- and reactive- power. Based on this, damping correction loop is designed to be more adaptive to the grid connected mode under power coupling condition.

The structure of GF-VSG with damping correction loop is shown in Fig. 1. The GF-VSG is connected to AC power

system through an L filter, R_f and L_f are the internal resistance and filter inductance, respectively. R_g and L_g represent the resistance and inductance of AC grid with line impedance, which can be used to describe the characteristic of the grid stiffness. The damping correction loop is inserted in the VSG control to provide additional inertia and damping support without change the structure of VSG control. i_{abc} and e_{abc} are the three-phase AC current and output voltage of inverter, respectively. i_d, i_q, e_d and e_q represent the corresponding current and voltage in dq coordinate system.

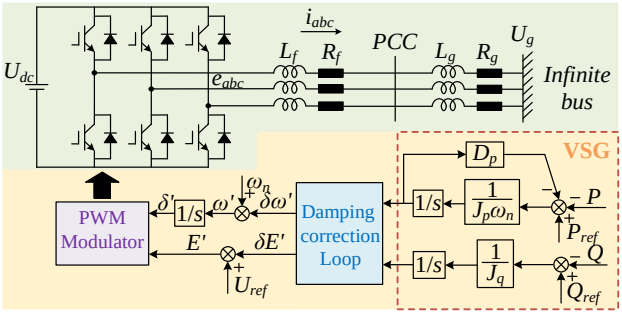

Fig. 1. Scheme diagram and VSG control of grid-forming inverter.

According to [20], the relationship among the grid current and voltage in synchronous rotating d-q frame, output voltage magnitude and phase-angle difference can be written as:

$$\begin{cases} f_1(i_d,\delta,E)=0 \\ f_2(i_q,\delta,E)=0 \end{cases} \tag{1}$$

$$\begin{cases} g_1(e_d,\delta,E)=0 \\ g_2(e_q,\delta,E)=0 \end{cases} \tag{2}$$

Based on the equations (1) and (2), the active- and reactive-power loops are coupled with each other in the dq-coordinate system. The relationship among P, Q, δ and E can be written as:

$$\begin{cases} P=1.5(e_d i_d+e_q i_q)G_l(s)=h_1(\delta,E) \\ Q=1.5(e_q i_d-e_d i_q)G_l(s)=h_2(\delta,E) \end{cases} \tag{3}$$

where P, Q, δ and E are the output active power, reactive power, phase-angle difference and voltage magnitude of the VSG, $G_l(s)$ is the low frequency.

Then, small signal model of active and reactive power is established and expressed as:

$$\begin{cases} \Delta P=\Delta P_\delta+\Delta P_E=G_{P\delta}(s)\Delta\delta+G_{PE}(s)\Delta E \\ \Delta Q=\Delta Q_\delta+\Delta Q_E=G_{Q\delta}(s)\Delta\delta+G_{QE}(s)\Delta E \end{cases} \tag{4}$$

where $G_{P\delta}(s)$, $G_{PE}(s)$, $G_{Q\delta}(s)$ and $G_{QE}(s)$ denote the transfer functions of interaction among output voltage magnitude, phase-angle difference, active and reactive power of the VSG.

To cope with the intractable challenges in frequency and voltage stability caused by the high permeability power electronics equipment. VSG control is adopted to improve the system inertia and damping effectively. The active power-frequency (P-f) loop and reactive power-voltage (Q-E) control loop are adopted to regulate the output phase angle and voltage magnitude of inverter. J_p and D_p are the inertia and damping coefficient of P-f loop, and J_q is the control parameter of Q-E loop. Then, the VSG control can be given by

$$\begin{cases} P_{ref}-P=D_p(\omega-\omega_n)+J_p\omega_n(\omega-\omega_n)s \\ Q_{ref}-Q=J_q(E-U_{ref})s \end{cases} \tag{5}$$

where P_{ref} and Q_{ref} are the references of active and reactive power. ω and ω_n are the angular frequency of the VSG and its reference value. U_{ref} is the nominal voltage magnitude.

The model is then linearized to derive a small signal model between active power and the output phase angle, reactive power and the voltage magnitude of VSG, and the expressions can be derived as:

$$\begin{cases} G_1(s)=\Delta\delta/(\Delta P_{ref}-\Delta P)=1/(J_p\omega_n s^2+D_p s) \\ G_2(s)=\Delta E/(\Delta Q_{ref}-\Delta Q)=1/J_q s \end{cases} \tag{6}$$

Comparing (4) with (6), the open-loop transfer function with the interaction of power coupling can be written as [20]:

$$G_{P\_open}(s)=G_1(s)\left[\frac{-G_{PE}(s)G_{Q\delta}(s)G_2(s)}{1+G_{QE}(s)G_2(s)}+G_{P\delta}(s)\right] \tag{7}$$

B. Operation Principle of Damping Correction Loop

To eliminate the sub-synchronous oscillation caused by the power coupling, damping correction loop is inserted in the VSG control. As illustrated in Fig.1, the damping correction loop is introduced to modify the virtual inertia and virtual damping of VSG, which is composed by a typical first order lag link. The transfer function can be obtained as:

$$T(s)=\frac{nTs+1}{Ts+1} \qquad (0<n<1) \tag{8}$$

where T and n are the time constant and lag coefficient of the first order lag model. The value of maximum-lag angle frequency ω_{Tmax} and maximum-lag magnitude L_{Tmax} are generally determined by the coefficients of T and n, given as:

$$\omega_{Tmax}=1/T\sqrt{n} \tag{9}$$

$$L_{Tmax}=20\lg n \tag{10}$$

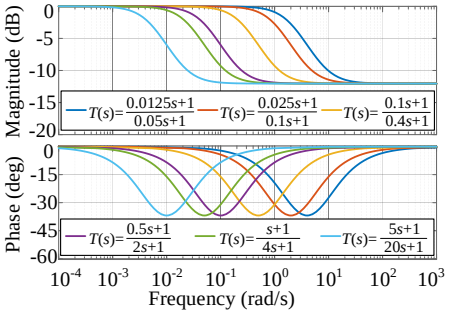

Fig.2. Bode diagram of $T(s)$ with different lag angle.

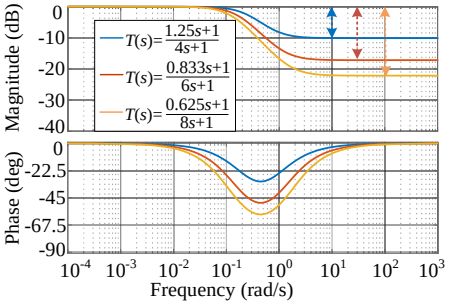

Fig.3. Bode diagram of $T(s)$ with different lag magnitude.

Keeping the maximum-lag magnitude L_{Tmax} constant, Fig. 2 depicts the characteristics of $T(s)$ changes with variation of T. As the constant time increases, the maximum-lag angle frequency ω_{Tmax} of $T(s)$ decreases accordingly, which mean that

the characteristics of phase within region of low-frequency change significantly. Similarly, keeping the maximum-lag angle frequency ω_{Tmax} constant, as observed from Fig. 3, the Bode of $T(s)$ with different lag magnitudes have similar frequency response when ω_T<0.28 rad/s. However, during the range of ω_T>20 rad/s, L_{Tmax} are -10.1dB, -17.15dB and -22.1dB, respectively. As the lag coefficient n decreases, the maximum-lag magnitude L_{Tmax} is gradually raised.

C. Damping Correction Loop Scheme Description

Aiming at the characteristic of VSG control, the damping correction loop can be described in a 2×1 matrix $\boldsymbol{T_{PQ}}$, i.e.,

$$\boldsymbol{T_{PQ}} = \begin{bmatrix} T_P(s) \\ T_Q(s) \end{bmatrix} \tag{11}$$

where $T_P(s)$ and $T_Q(s)$ are the damping correction term in active- and reactive-power loop, respectively.

With the help of damping correction loop, the reconfiguration of VSG control is achieved, thus the system open loop transfer function is available by giving a certain expression $\boldsymbol{T_{PQ}}$.

$$G_{P\_open\_T}(s) = G_1(s)\left[\frac{-G_{PE}(s)G_{Q\delta}(s)G_2(s)T_Q(s)}{1+G_{QE}(s)G_2(s)T_Q(s)} + G_{P\delta}(s)\right]T_P(s) \tag{12}$$

Note that the damping correction loop $\boldsymbol{T_{PQ}}$ is usually used to improve the performance of the system phase margin by decreasing the cut-off frequency of the system. To achieve this goal, ω_{Tmax} should be designed less than the system cut-off frequency ω_o, resulting in an increase in system phase margin.

According to the above analysis, the requirement of $\omega_{Tmax}<\omega_o/10$ should be meet. Then the magnitude of open-loop transfer function in ω_{on} with the damping correction loop is expressed as follows:

$$L(\omega_{on}) = \sqrt{(\mathrm{Re}[G_{p\_open\_T}(s)]\big|_{s=j\omega_{on}})^2 + (\mathrm{Im}[G_{p\_open\_T}(s)]\big|_{s=j\omega_{on}})^2} \tag{13}$$

where ω_{on} is new cut-off frequency with $\boldsymbol{T_{PQ}}$.

Therefore, the phase angle increment of the system produced by $\boldsymbol{T_{PQ}}$ can be obtained as:

$$\varphi_c = \arctan\frac{\mathrm{Im}[G_{p\_open\_T}(s)]}{\mathrm{Re}[G_{p\_open\_T}(s)]}\bigg|_{s=j\omega_{on}} - \arctan\frac{\mathrm{Im}[G_{p\_open}(s)]}{\mathrm{Re}[G_{p\_open}(s)]}\bigg|_{s=j\omega_o} \tag{14}$$

To fulfill the expectation, the damping correction loop scheme for GF-VSG is necessary. As illustrated in Fig.1, the controller $\boldsymbol{T_{PQ}}$ is added in the power loop. In this part, the control constructure of damping correction loop is discussed to clarify the effect of $\boldsymbol{T_{PQ}}$.

Here, a comparative stability analysis is developed with four different damping correction loops for selecting the optimal structure, which aims to attain good stability margins. Fig. 3 gives the frequency response characteristics changes among different cases with $T(s)=(s+1)/(4s+1)$. In Fig. 4, four cases were carried out to research the optimal structure of damping correction loop, which can be written in $T_P(s)$ and $T_Q(s)$.

Case 1: $T_P(s)=0$, and $T_Q(s)=0$.
Case 2: $T_P(s)=T(s)$, and $T_Q(s)=0$.
Case 3: $T_P(s)=0$, and $T_Q(s)=T(s)$.
Case 4: $T_P(s)=T(s)$, and $T_Q(s)=T(s)$.

The effect of $\boldsymbol{T_{PQ}}$ is clarified in this part, a 34.91 deg leading change of phase margin is achieved after the damping correction in active power loop is activated. It should be noted that the stability of the grid-connected system is enhanced more significantly when the damping correction loop is deployed in the active power loop. In case 3, the same $T(s)$ is developed in both active- and reactive-power loop. Comparing to case 2, the result indicates that $T_Q(s)$ has little help to improve the system stability with only 0.75 deg increment of phase margin. In addition, the bode result of case 4 was almost the same as that of case 2, which indicates that the system stability is guaranteed only with an active power damping correction.

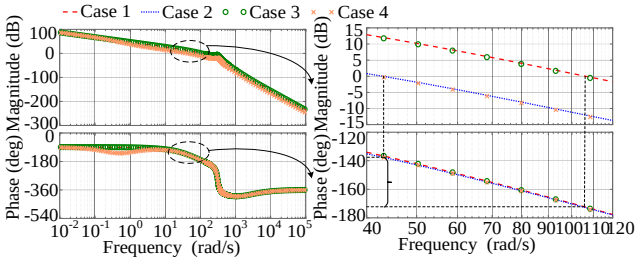

Fig. 4. Bode diagram of different types of damping correction loop.

III. Stability Analysis of Damping Correction Loop for GF-VSG

The stability analysis of damping correction loop and design principle is illustrated in this section. In order to show a comprehensive discussion of the proposed control, the effect of synchronization, damping and inertia have been clarified.

A. Impact of Damping Correction Loop into VSG on Stability Analysis

The angular difference between voltages impacts the system stability, which is defined by the short circuit ratio (SCR) and R_g/X_g ratio. As well-known, SCR is usually used to describe the grid strength. In recent years, many researches have focused on the impact of SCR to power system dynamic performance. Nevertheless, the R_g/X_g also plays a significant role in the system stability analysis with damping correction.

To fulfill the desirable damping correction effect, the power compensation effect is demonstrated in bode diagrams as shown in Fig. 5 for different D_p, J_p and R_g/X_g. The robustness performance with phase margin increment (PMI) in different D_p, J_p and R_g/X_g have been summarized in table I. As observed, $G_{p\_open}(s)$ and $G_{p\_open\_T}(s)$ have similar phase-frequency characteristics in whole frequency band with different D_p and R_g/X_g. However, the magnitude-frequency characteristics are different except in low-frequency band, the PMI is 21.33 deg at D_p=94.25 when $T_P(s)=(1.25s+1)/(4s+1)$ is inserted in active power loop. With an increase in D_p=219.91, the PMI is 32.21 deg. As per Fig. 4(b), stability analysis is developed for various J_p. Different from D_p and R_g/X_g, the characteristics of both magnitude-frequency and phase-frequency are changed when J_p raised from 0.01 to 0.25. As for the phase-frequency response, the characteristics in high-frequency band are almost unchanged no matter what J_p is. In addition, the effect of damping correction is decreased significantly, but not abolished completely. According to Fig. 5(c), the magnitude

frequency response has remained the same for different R_g/X_g. The relative stability is enhanced with the introduction of damping correction loop, and similar PMI is observed as R_g/X_g increasing from 0.3 to 0.5, where PMI is approximately 31 deg.

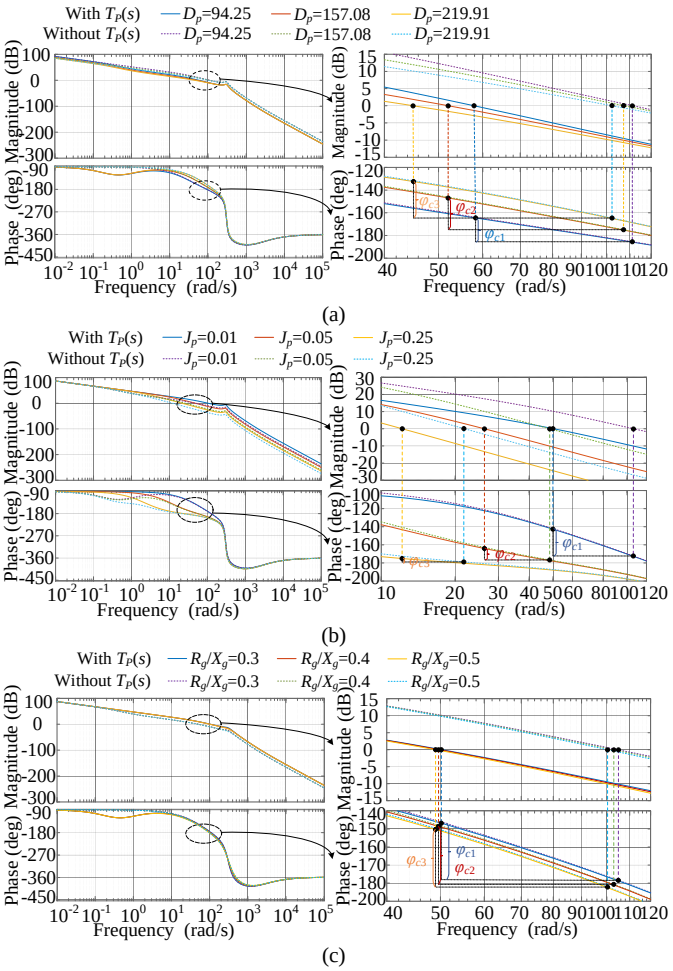

Fig. 5. Bode diagram of open loop transfer function with and without damping correction loop. (a) Changing of D_p. (b) Changing of J_p. (c) Changing of R_g/X_g.

TABLE I

PARAMETERS & PERFORMANCE

Parameter	Range	Phase Margin increment	Performance
D_p	94.25	21.33°	Good
	157.08	28.17°	Excellent
	219.91	32.21°	Excellent
J_p	0.01	29.49°	Excellent
	0.05	12.68°	Medium
	0.25	3.85°	Pass
R_g/X_g	0.3	31.50°	Excellent
	0.4	31.92°	Excellent
	0.5	31.93°	Excellent

To demonstrate the improvement of system dynamic characteristics, Fig. 6 depicts the bode diagram of $G_{p\_open\_T}(s)$ with variation of L_{Tmax} at ω_{Tmax}>0.4 rad/s. As the maximum-lag magnitude increases, the magnitude-frequency curve is gradually declined, and the PMI is increased. Specifically, the PMI is 29.48 deg at 50.4 rad/s, and increase to 57.02 deg at 16.43 rad/s. Therefore, the additional damping is generated and the stability is strengthened effectively.

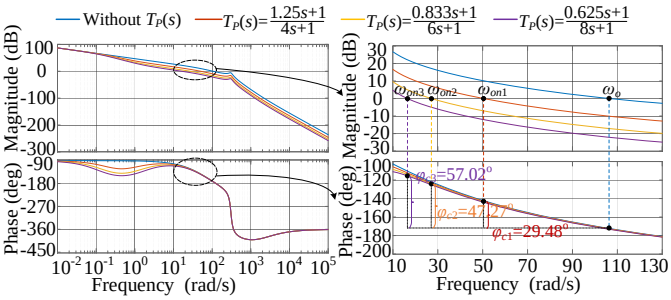

Fig. 6. Bode diagram of $G_{p\_open\_T}(s)$ with different L_{Tmax}.

B. Damping and Synchronization Effect of Damping Correction Loop

In this section, the damping correction loop provide positive damping and synchronization to enhance the frequency stability in difference cases. From physical perspective of damping and synchronization, the active power is composed of power-angle related part (PARP) (ΔP_δ), voltage-coupling related part (VCRP) (ΔP_E) and damping part (ΔP_D) [20]. The open-loop transfer function of the system with damping correction loop is formulated by (12) in part A, and it can be represented as

$$G_{P\_open\_T}(s)=G_1(s)\left[\frac{-G_{PE\_T}(s)G_{Q\delta\_T}(s)G_2(s)}{1+G_{QE\_T}(s)G_2(s)}+G_{P\delta\_T}(s)\right] \quad (15)$$

where $G_{P\delta\_T}(s)$, $G_{PE\_T}(s)$, $G_{Q\delta\_T}(s)$ and $G_{QE\_T}(s)$ can be given by

$$\begin{cases} G_{P\delta\_T}(s)=G_{P\delta}(s)T_P(s) \\ G_{PE\_T}(s)=G_{PE}(s)T_P(s) \\ G_{Q\delta\_T}(s)=G_{P\delta}(s)T_Q(s) \\ G_{QE\_T}(s)=G_{PE}(s)T_Q(s) \end{cases} \quad (16)$$

From (15) and (16), the damping correction loop can be recognized as a reshaping part in power coupling. Therefore, the effect of damping and synchronization obtained from damping correction loop can be reflected in PARP and VCRP, which can be expressed as:

$$\begin{cases} h_{E\_T}(s)=-G_{PE\_T}(s)G_{Q\delta\_T}(s)G_2(s)/\left(1+G_{QE\_T}(s)G_2(s)\right) \\ h_{\delta\_T}(s)=G_{P\delta\_T}(s) \end{cases} \quad (17)$$

where ΔP_{δ_T} and ΔP_{E_T} are the PARP and VCRP with $\boldsymbol{T_{PQ}}$. $h_{\delta\_T}(s)$ and $h_{E\_T}(s)$ are the transfer functions from ΔP_{δ_T} and ΔP_{E_T} to $\Delta\delta$, respectively.

The damping part is only determined by virtual damping, so the transfer function from total active power with damping correction loop (ΔP_{total_T}) to angle difference ($\Delta\delta$) can be written as:

$$h_{total\_T}(s)=h_{E\_T}(s)+h_{\delta\_T}(s)+h_D(s) \quad (18)$$

Since the scheme of damping correction loop on system stability is analyzed detailed in section II, case 2 is selected to show the characteristic of damping correction. Fig. 7 displays the bode diagram of the designed $h_{\delta\_T}(s)$, $h_{E\_T}(s)$, $h_D(s)$, $h_{total\_T}(s)$ and the corresponding active power vector with damping correction loop, where D_p=94.25. From Fig. 7, the vector of ΔP_{total_T} is located in the first quadrant, which means that total

damping and synchronization component are positive and it remains in stable region. It is different from traditional VSG control, which is in the fourth quadrant. The analytical result is consistent with the purple dotted line in Fig. 5(a).

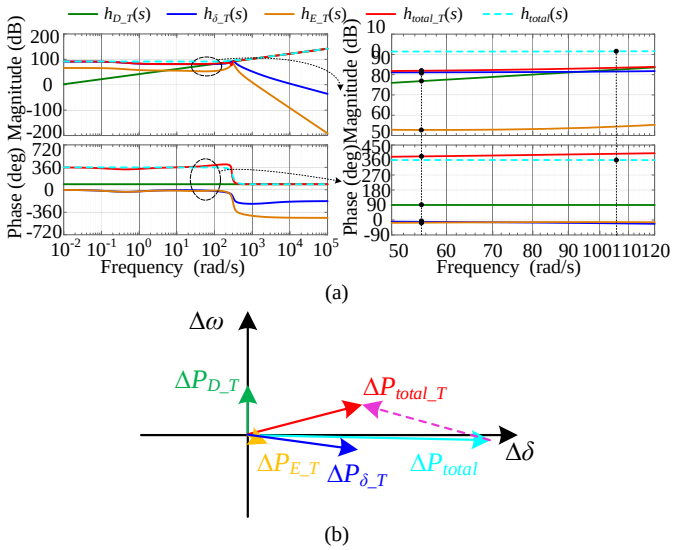

Fig. 7. Bode diagram and vector diagram with damping correction loop in low D_p. (a) Bode diagram. (b) Vector.

Similar analysis has been performed for high R_g/X_g on the impact of stability of damping and synchronization. Fig. 8 displays the bode diagram and corresponding vector for damping correction loop on R_g/X_g=0.5. As per Fig. 8, the vector of ΔP_{total_T} move towards the first quadrant with the damping correction loop inserted. From the view of damping and synchronization, the damping correction loop reduces the negative damping originated from strong coupling effect between active- and reactive-power. In the meantime, the positive synchronization component is also be weakened, but the total synchronization part still maintained positive. The proposed damping correction loop on high R_g/X_g reflects satisfactory gain and phase margin in Fig. 8(b), which is in line with the analysis result in Fig. 5(c).

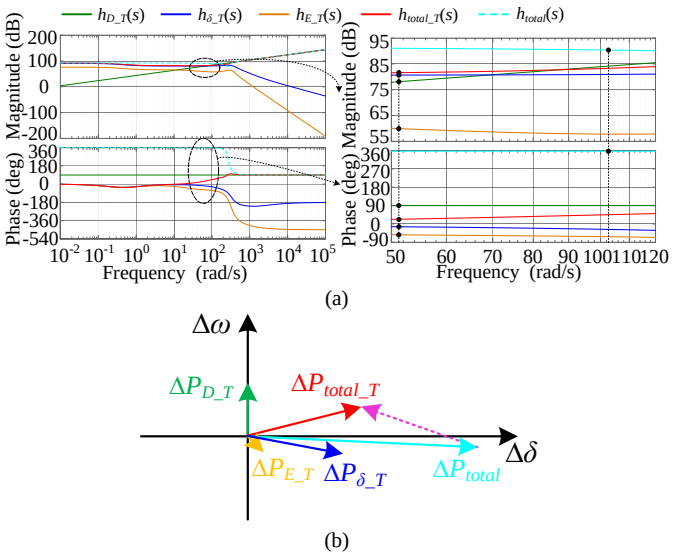

Fig. 8. Bode diagram and vector diagram with damping correction loop in high R_g/X_g. (a) Bode diagram. (b) Vector.

C. Equivalent Damping and Equivalent Inertia Effect of Damping Correction Loop

The impact of the proposed correction damping loop has been researched in equivalent virtual damping and virtual inertia as well as stability analysis. Since control parameters in reactive power loop are ultra-insensitive, the influence of damping correction with $T_Q(s)$ can be ignored as shown in section II, thus the damping correction loop in reshaping equivalent virtual damping and virtual inertia can be reduced by eliminating $T_Q(s)$, as illustrated by

$$G_{1\_T}(s) = G_1(s)T_P(s) = \frac{1+nTs}{(J_p\omega_n s^2 + D_p s)(1+Ts)} \tag{19}$$

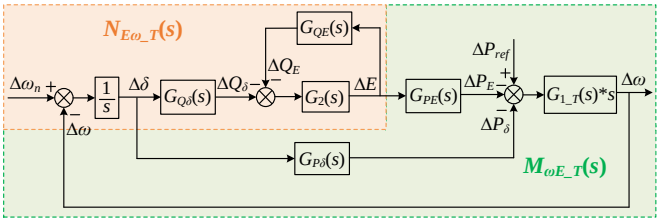

Fig. 9. Relationship between $\Delta E_{\_T}$ and $\Delta\omega_{\_T}$ with damping correction loop.

According to the feedback effect between frequency and magnitude of VSG output voltage in Fig. 9 [20], the coupling terms of $M_{\omega E\_T}(s)$ and $N_{E\omega\_T}(s)$ responding to equivalent damping and equivalent inertia can be given by

$$M_{\omega E\_T}(s) = \frac{\Delta\omega_{\_T}}{\Delta E_{\_T}} = \frac{-G_{PE}(s)G_{1\_T}(s)s}{1+G_{1\_T}(s)G_{P\delta}(s)} \tag{20}$$

$$N_{E\omega\_T}(s) = \frac{\Delta E_{\_T}}{\Delta\omega_{\_T}} = \frac{-G_{Q\delta}(s)G_2(s)/s}{1+G_2(s)G_{QE}(s)} \tag{21}$$

where $M_{\omega E\_T}(s)$ and $N_{E\omega\_T}(s)$ are transfer functions flowing from $\Delta E_{\_T}$ to $\Delta\omega_{\_T}$ and from $\Delta\omega_{\_T}$ to $\Delta E_{\_T}$, respectively.

This part will evaluate the system stability by the negative feedback-based frequency analytical method. The relationship of $\Delta\omega$ between $(i+1)^{\text{th}}$ and i^{th} instant can be expressed as

$$G_{couple\_T}(s) = \frac{G_{PE}(s)G_{Q\delta}(s)G_{1\_T}(s)G_2(s)}{\left[1+G_{1\_T}(s)G_{P\delta}(s)\right]\left[1+G_2(s)G_{QE}(s)\right]} \tag{22}$$

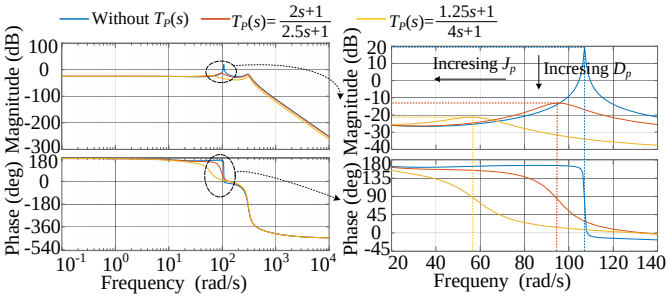

Fig. 10. Bode diagrams of $G_{couple\_T}(s)$ for different $T_P(s)$.

Fig. 10 visualizes the equivalent virtual damping and virtual inertia of the proposed damping correction loop. A resonance peak of $G_{couple\_T}(s)$ is appeared in the condition of weak damping without $T_P(s)$, but the damping correction in active power control loop attenuates the resonance peak, especially for the negative damping effect caused by the power coupling. As illustrated, the decrease of lag coefficient n will gradually enhance the system damping and inertia, thereby indicating that

the stability of grid-connected system may be improved by the introduced damping correction loop, reshaping the conventional VSG control scheme.

To further identify the equivalent inertia and equivalent damping created by damping correction loop, the damping correction is implemented in the active power [23]. The rearranged $G_{1\_T}(s)$ can be decomposed into real and imaginary components in virtual damping and virtual inertia at critical frequency ω_c.

$$G_{1\_T}(s)\Big|_{s=j\omega_c} = G_{real\_T}(D_p^0, J_p^0) + jG_{imag\_T}(D_p^0, J_p^0) \quad (23)$$

where D_p^0 and J_p^0 are the initial virtual damping and inertia.

Similarly, the reshaping effect of $T_P(s)$ can be regarded as a substitution of equivalent damping (δD_p^T) and equivalent inertia (δJ_p^T) compensation. Substituting s=jω_c, the active power part of (6) with damping correction loop can be written as

$$G_1(s)\Big|_{s=j\omega_c} = G_{real}(D_P^T, J_P^T) + jG_{imag}(D_P^T, J_P^T) \quad (24)$$

where D_p^T and J_p^T are the equivalent damping and equivalent inertia after the introduction of $T_P(s)$.

According to (23) and (24), the D_p^T and J_p^T can be calculated by

$$G_{1\_T}(D_p^0, J_p^0) = G_1(D_p^T, J_p^T) \quad (25)$$

Then the increment of equivalent damping and inertia provided by $T_P(s)$ can be obtained by

$$\begin{cases} \delta D_P^T = D_P^T - D_p^0 \\ \delta J_P^T = J_P^T - J_p^0 \end{cases} \quad (26)$$

Relative stability analysis with equivalent damping and equivalent inertia has been explored for different $T_P(s)$. In order to describe the characteristic of equivalent damping and inertia provided by $T_P(s)$ more intuitively, taking the initial parameters (D_p^0 and J_p^0) initialized in (1,1), thus D_p^T and J_p^T can be expressed as per unit value too. Fig. 11 shows vector diagram of equivalent damping and equivalent inertia for different $T_P(s)$. When $T_P(s)$=(0.625s+1)/(8s+1), the equivalent damping and inertia increases from 1 to 12.35 and from 1 to 16.51, respectively. There is no doubt that D_p^T and J_p^T tend to be increasing along with the lag coefficient n decreased. As for $T_P(s)$=(1.25s+1)/(4s+1), D_p^T is almost synchronized with the growth of J_p^T. However, with the decrease of n, the deviation of increasing rate of D_p^T and J_p^T are gradually appeared, which shows more significant in J_p^T.

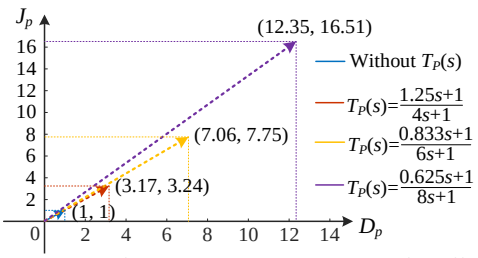

Fig. 11. Vector diagram of equivalent damping and inertia for different $T_P(s)$.

What's more, Fig.11 shows that the corresponding magnification is about 1/n times the original initial size. Yet it's worth noting that the vector formed by updated virtual damping and virtual inertia to partially moving with further reduction of n. That is, the virtual damping and virtual inertia increased with different growth rates of n, the lower n resulted in rapid deviation of the initial vector.

The effect of synchronization, damping and inertia of damping correction loop have been validated in the above analysis. There is no doubt that the updated virtual damping and virtual inertia tend to be increasing along with the lag coefficient decreased, and increase simultaneously with the damping correction loop. Besides, with the proposed damping correction loop, the synchronization component is reduced at a certain extent, while the total synchronization effect still maintains positive.

D. Design of Damping Correction Loop Scheme

In this part, the architecture of $\boldsymbol{T_{PQ}}$ is designed to achieve the desired dynamic performance. Before designing the controller, it is necessary to reasonably coordinate the positive damping component and negative synchronization component of the damping correction loop. Keeping the maximum-lag angle frequency ω_{Tmax} as constant, vectors of each active power components are demonstrated for different values of n and T as shown in Fig. 12.

It is observed that ΔP_{total} for $T_{P1}(s)$ and $T_{P2}(s)$ are located in the first quadrant, which different from ΔP_{total0} in fourth quadrant without $T_P(s)$. From Fig. 12, the damping and synchronization effect of ΔP_{total} are mainly determined by the magnitude-phase characteristics of $h_\delta(s)$. The damping correction loop reduce the magnitude and phase of $h_\delta(s)$ at ω_c. Therefore, the negative damping and positive synchronization component of ΔP_δ are decreased at the same time. In summary, damping correction loop plays a significant role in the stability analysis, due to the conflict between positive damping and negative synchronization of $T_P(s)$, the damping correction loop needs to be configured with a suitable stability margin.

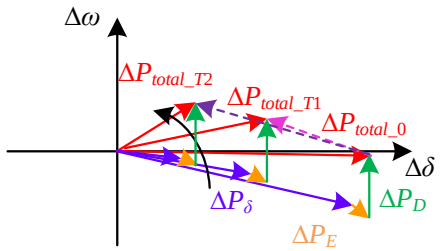

Fig. 12. Vector diagrams of ΔP_{total_T} for different $T_P(s)$.

With the configured positive damping and negative synchronization, the design and application procedure of the proposed damping correction loop is illustrated in Fig. 13, which can be summarized as follows:

(1) Initially, the desired parameter of L-filter should be determined.

(2) Calculate the initial open-loop cutoff frequenc, according to the desired phase margin, a phase compensation is set, and then the updated open-loop cutoff frequency can be obtained.

(3) Display the magnitude (L_T) of open-loop transfer function at ω_{on}, thereby parameter n can be determined by equation (10).

(4) Define ω_{Tmax}<ω_{on}/10, and obtain the minimum of T, calculate the equivalent damping D_p^T and equivalent inertia J_p^T then judge whether D_p^T and J_p^T can meet a few key benchmarks for a preliminary result. If not, increasing n, and thereby obtain

an updated ω_{on}.

(5) Obtain the required T and n, and describe the bode diagram of $G_{p\_open\_T}(s)$ for phase margin validation, check whether the phase margin is obeyed. If not, increasing T until the result is satisfied. Subsequently, describe the electromagnetic transient of frequency with overshoot f_m and attenuation time t_a to achieve the desired dynamic performance, T and n are updated again until the logicality can be satisfied.

(6) Simulations and experiments for further verification, and damping correction loop is correct and effective.

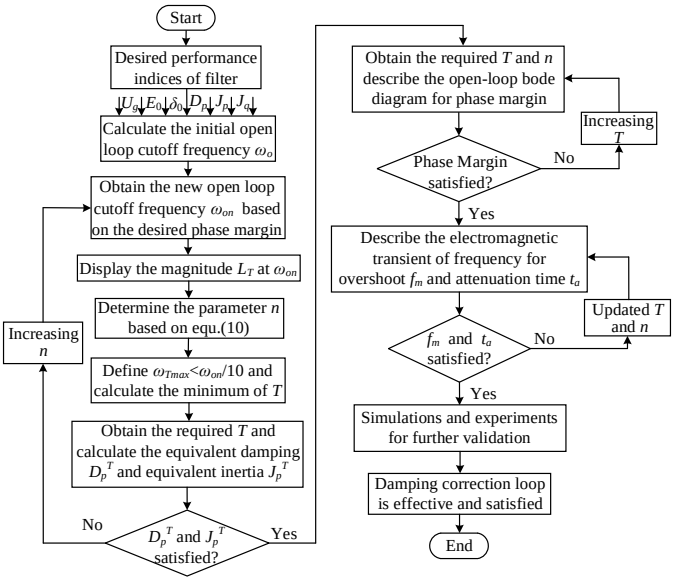

Fig. 13. Flowchart describing design principle and the implementation of the damping correction loop.

IV. Experimental Verification

To further validate the effectiveness of damping correction loop, experiments are carried out based on the system schematic shown in Fig. 1. The indices of damping correction loop are different in following cases, and the details are introduced in the next corresponding part.

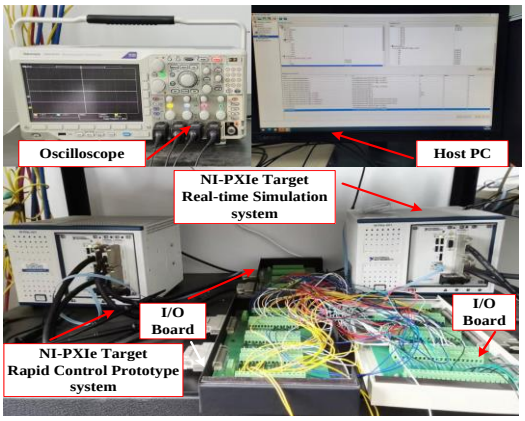

Fig. 14. Star-Sim experimental setups.

Two variations of R_g/X_g are taken into account to validate the improved phase margin with the proposed damping correction loop. Fig. 15 illustrates the experimental results of P, Q, f and i_{abc} with and without the proposed damping correction loop. At R_g/X_g =0.108, the system is stable with a good dynamic response. For the same control parameters at R_g/X_g =0.4, the system is unstable with negative phase margin of −0.63 deg which can be found in Fig. 5(c). However, when damping correction loop $T_P(s)$=(1.25s+1)/(4s+1) is inserted in active power control framework, the system stability is enhanced with an improved phase margin of 31.29 deg, also found in Fig. 5(c) with yellow dotted line. Based on this, the feasibility and effectiveness of the proposed damping correction loop was validated by the experimental results.

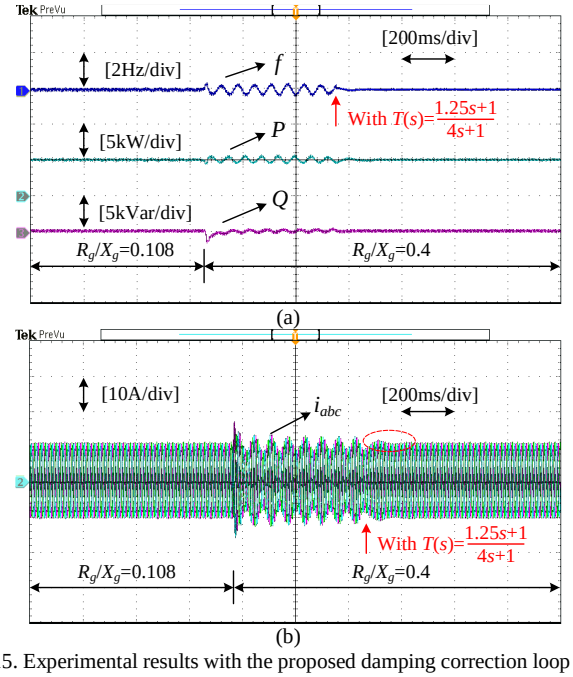

Fig. 15. Experimental results with the proposed damping correction loop under R_g/X_g disturbance. (a) P, Q, f. (b) i_{abc}.

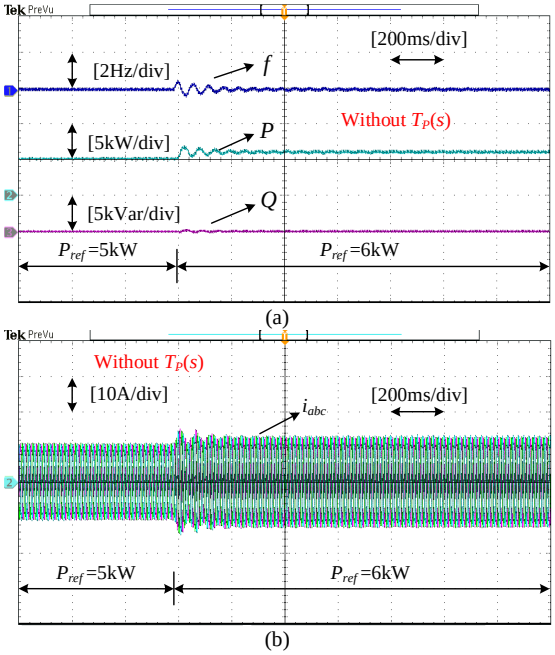

Fig. 16. Experimental results without damping correction loop. under the active power disturbance (a) P, Q, f. (b) i_{abc}.

To illustrate the applicability of proposed damping correction loop for realizing the sufficient damping and inertia support, Fig. 16- Fig. 18 show the experimental results with and without the proposed control when active power changes. In these cases, the ratio of R_g/X_g is set as 0.108 and held constant.

Initially, the proposed power compensation control is disabled. It is observed in Fig. 16 that the stability of grid-connected system is well guaranteed even the controller undergoes a disturbance with 20% (1kW) active power reference step changes. Though certain overshoots of 0.5Hz and sub-synchronous oscillations do exist. About 0.3s later, sub-synchronous attenuation oscillation disappears in the waveform of VSG output frequency, powers as well as grid-connected current.

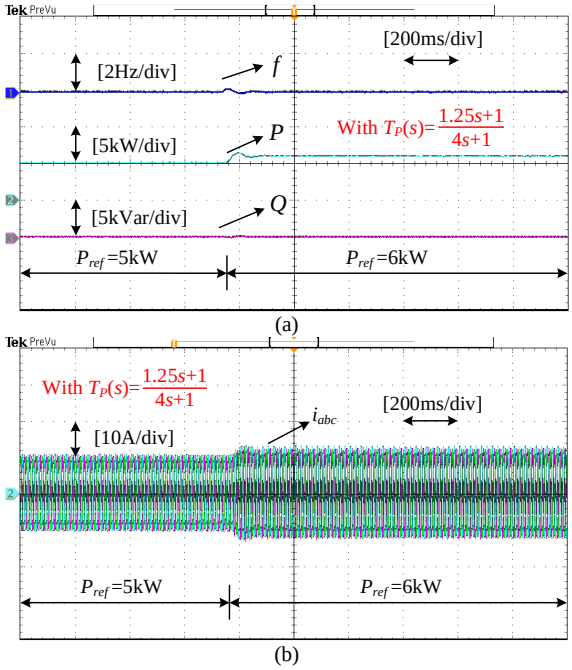

Fig. 17. Experimental results with $T_P(s)=(1.25s+1)/(4s+1)$ under the active power disturbance. (a) *P*, *Q*, *f*. (b) i_{abc}.

Next, the active power disturbance test is also developed to validate the stability margin of the system with damping correction loop. From Fig. 17 and Fig. 18, the active power reference step from 5kW to 6kW. In these cases, the weak sub-synchronous oscillation can be mitigated quickly with the proposed power compensation control and arrived at the steady state within 0.1s when $T_P(s)=(1.25s+1)/(4s+1)$ as shown in Fig. 17. It should be noted that the selected scheme of $T_P(s)$ for the system damping correction is effective since the maximum frequency nadir is only 0.15 Hz which does not exceed the allowable limit ($\pm$0.2 Hz).

To further evaluate the equivale ent damping and inertia emulation with consideration of the damping correction loop, Fig. 18 shows the dynamic response of *P*, *Q*, *f* and i_{abc} under the active power disturbance. Similarly, it takes shorter time than we expect to converge to a steady state. When $T_P(s)=(0.833s+1)/(6s+1)$, the fluctuation of power, frequency and grid-connected current respond to their given reference smoothly with little or no overshoot. Therefore, the stability of the system has been improved significantly, and the damping correction effect is validated. From Fig.16- Fig.18, there was little change in reactive power when 20% active power reference step change. The deviation of reactive power was caused by the coupling degree between active- and reactive-power. As the ratio of resistance to inductance is small, the reactive power would converge to 0 Var without any steady-state error.

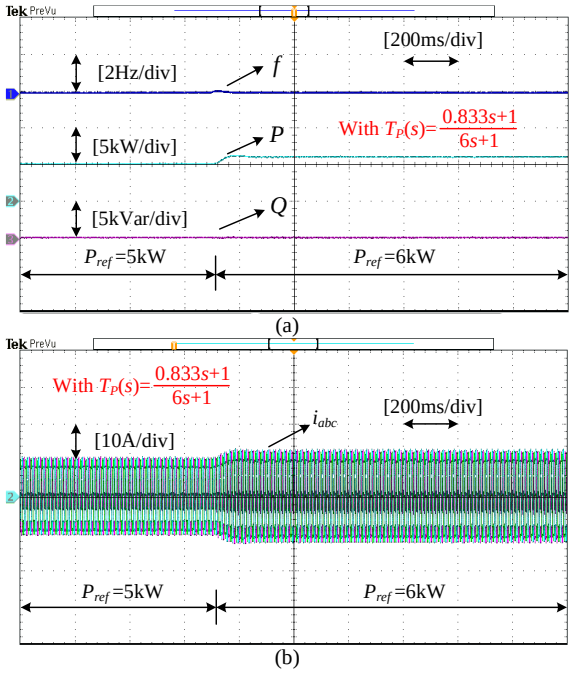

Fig. 18. Experimental results with $T_P(s)=(0.833s+1)/(6s+1)$ under the active power disturbance. (a) *P*, *Q*, *f*. (b) i_{abc}.

The above experimental results suggest that the proposed generic power compensation control plays a significant role in the stability of the system and a satisfactory stability margin is achieved with damping correction loop

V. Conclusions

In this paper, a damping correction loop based on VSG for grid-connected power converter with high penetration of RESs is proposed to provide additional damping and inertia support. Sub-synchronous oscillation caused by the active- and reactive-power coupling in weak damping condition has been suppressed. The conclusions are summarized as follows:

(1) The scheme of damping correction loop is investigated, and the system stability margin can be guaranteed well only with damping correction in active power control loop. The proposed control method can be easily implemented and applied to various operating conditions.

(2) The damping correction loop reshapes the damping and synchronization of GF-VSG from the fourth quadrant into the first quadrant within the sub-synchronous frequency band under high R_g/X_g and weak damping condition. From another aspect, the equivalent damping and inertia provision ability are enhanced after the damping correction loop is inserted.

(3) The negative damping effect has been removed by the proposed damping correction loop, and the frequency nadir and rate of change of frequency can be limited within the frequency thresholds under system disturbance. In addition, the reactive power converged to 0 Var without any steady-state error under various cases. Experimental results validate the effectiveness of the damping correction loop for improving the dynamic performance of the GF-VSG.

REFERENCES

[1] F. Blaabjerg and K. Ma, "Future on Power Electronics for Wind Turbine Systems," *IEEE Journal of Emerging and Selected Topics in Power Electronics*, vol. 1, no. 3, pp. 139-152, Sept. 2013.

[2] Z. Shuai, W. Huang, and Z. J. Shen, "Active Power Oscillation and Suppression Techniques Between Two Parallel Synchronverters During Load Fluctuations," *IEEE Transactions on Power Electronics*, vol. 35, no. 4, pp. 4127-4142, April 2020.

[3] A. Asrari, M. Mustafa, M. Ansari and J. Khazaei, "Impedance Analysis of Virtual Synchronous Generator-Based Vector Controlled Converters for Weak AC Grid Integration," *IEEE Transactions on Sustainable Energy*, vol. 10, no. 3, pp. 1481-1490, July 2019.

[4] W. Wu, L. Zhou, and Y. Chen, "Sequence-Impedance-Based Stability Comparison Between VSGs and Traditional Grid-Connected Inverters," *IEEE Transactions on Power Electronics*, vol. 34, no. 1, pp. 46-52, Jan. 2019.

[5] M. Saeedian, B. Eskandari, S. Taheri, M. Hinkkanen and E. Pouresmaeil, "A Control Technique Based on Distributed Virtual Inertia for High Penetration of Renewable Energies Under Weak Grid Conditions," *IEEE Systems Journal*, vol. 15, no. 2, pp. 1825-1834, June 2021.

[6] J. Liu, Y. Miura and T. Ise, "Fixed-Parameter Damping Methods of Virtual Synchronous Generator Control Using State Feedback," in *IEEE Access*, vol. 7, pp. 99177-99190, 2019.

[7] M. Saeedian, R. Sangrody, M. Shahparasti, S. Taheri and E. Pouresmaeil, "Grid – Following DVI – Based Converter Operating in Weak Grids for Enhancing Frequency Stability," *IEEE Transactions on Power Delivery*, vol. 37, no. 1, pp. 338-348, Feb. 2022.

[8] J. Khazaei, Z. Tu and W. Liu, "Small-Signal Modeling and Analysis of Virtual Inertia-Based PV Systems," *IEEE Transactions on Energy Conversion*, vol. 35, no. 2, pp. 1129-1138, June 2020.

[9] Q. Peng, J. Fang, Y. Yang, T. Liu and F. Blaabjerg, "Maximum Virtual Inertia From DC-Link Capacitors Considering System Stability at Voltage Control Timescale," *IEEE Journal on Emerging and Selected Topics in Circuits and Systems*, vol. 11, no. 1, pp. 79-89, March 2021.

[10] M. Baruwa and M. Fazeli, "Impact of Virtual Synchronous Machines on Low-Frequency Oscillations in Power Systems," *IEEE Transactions on Power Systems*, vol. 36, no. 3, pp. 1934-1946, May 2021.

[11] L. Huang, H. Xin and Z. Wang, "Damping Low-Frequency Oscillations Through VSC-HVdc Stations Operated as Virtual Synchronous Machines," in IEEE Transactions on Power Electronics, vol. 34, no. 6, pp. 5803-5818, June 2019.

[12] Z. Qu, J. C. -H. Peng, H. Yang and D. Srinivasan, "Modeling and Analysis of Inner Controls Effects on Damping and Synchronizing Torque Components in VSG-Controlled Converter," *IEEE Transactions on Energy Conversion*, vol. 36, no. 1, pp. 488-499, March 2021.

[13] C. Li, Y. Yang, N. Mijatovic and T. Dragicevic, "Frequency Stability Assessment of Grid-Forming VSG in Framework of MPME With Feedforward Decoupling Control Strategy," in IEEE Transactions on Industrial Electronics, vol. 69, no. 7, pp. 6903-6913, July 2022.

[14] M. A. Torres, R. Tonkoski and C. R. Baier, "Operating Region of a Genset-Based Virtual Synchronous Generator," *IEEE Access*, vol. 8, pp. 136382-136392, 2020.

[15] J. Fang, Y. Tang, H. Li and X. Li, "A Battery/Ultracapacitor Hybrid Energy Storage System for Implementing the Power Management of Virtual Synchronous Generators," *IEEE Transactions on Power Electronics*, vol. 33, no. 4, pp. 2820-2824, April 2018.

[16] L. Li, Y. Sun, M. Su and S. Fu, "Decentralized Mutual Damping Control of Cascaded-Type VSGs for Power and Frequency Oscillation Suppression," *IEEE Transactions on Industrial Electronics*, vol. 69, no. 10, pp. 10215-10226, Oct. 2022.

[17] M. N. Ambia, K. Meng, W. Xiao, A. Al-Durra and Z. Y. Dong, "Interactive Grid Synchronization-Based Virtual Synchronous Generator Control Scheme on Weak Grid Integration," *IEEE Transactions on Smart Grid*, vol. 13, no. 5, pp. 4057-4071, Sept. 2022.

[18] B. Long, S. Zhu, J. Rodriguez, J. M. Guerrero and K. T. Chong, "Enhancement of Power Decoupling for Virtual Synchronous Generator: A Virtual Inductor and Virtual Capacitor Approach," *IEEE Transactions on Industrial Electronics*, vol. 70, no. 7, pp. 6830-6843, July 2023.

[19] X. Xiong, Y. Zhou, B. Luo, P. Cheng and F. Blaabjerg, "Analysis and Suppression Strategy of Synchronous Frequency Resonance for Grid-Connected Converters With Power-Synchronous Control Method," *IEEE Transactions on Power Electronics*, vol. 38, no. 6, pp. 6945-6955, June 2023.

[20] Y. Yang, J. Xu, C. Li, W. Zhang, Q. Wu, M. Wen, F. Blaabjer, "A New Virtual Inductance Control Method for Frequency Stabilization of Grid-Forming Virtual Synchronous Generators," *IEEE Transactions on Industrial Electronics*, vol. 70, no. 1, pp. 441-451, Jan. 2023.

[21] M. Li, Y. Wang, Y. Liu, N. Xu, S. Shu and W. Lei, "Enhanced Power Decoupling Strategy for Virtual Synchronous Generator," *IEEE Access*, vol. 8, pp. 73601-73613, 2020.

[22] O. Stanojev, U. Markovic, P. Aristidou and G. Hug, "Improving Stability of Low-Inertia Systems using Virtual Induction Machine Synchronization for Grid-Following Converters," *IEEE Transactions on Power Systems*, vol. 38, no. 3, pp. 2290-2303, May 2023.

[23] C. Li, Y. Yang, Y. Cao, A. Aleshina, J. Xu and F. Blaabjerg, "Grid Inertia and Damping Support Enabled by Proposed Virtual Inductance Control for Grid-Forming Virtual Synchronous Generator," *IEEE Transactions on Power Electronics*, vol. 38, no. 1, pp. 294-303, Jan 2023.

[24] T. Shintai, Y. Miura and T. Ise, "Oscillation Damping of a Distributed Generator Using a Virtual Synchronous Generator," in IEEE Transactions on Power Delivery, vol. 29, no. 2, pp. 668-676, April 2014.

[25] J. Alipoor, Y. Miura and T. Ise, "Power System Stabilization Using Virtual Synchronous Generator With Alternating Moment of Inertia," in IEEE Journal of Emerging and Selected Topics in Power Electronics, vol. 3, no. 2, pp. 451-458, June 2015.

[26] D. Li, Q. Zhu, S. Lin and X. Y. Bian, "A Self-Adaptive Inertia and Damping Combination Control of VSG to Support Frequency Stability," in IEEE Transactions on Energy Conversion, vol. 32, no. 1, pp. 397-398, March 2017.

[27] J. Chen and T. O'Donnell, "Parameter Constraints for Virtual Synchronous Generator Considering Stability," in IEEE Transactions on Power Systems, vol. 34, no. 3, pp. 2479-2481, May 2019.

[28] T. Wen, D. Zhu, X. Zou, B. Jiang, L. Peng and Y. Kang, "Power Coupling Mechanism Analysis and Improved Decoupling Control for Virtual Synchronous Generator," in IEEE Transactions on Power Electronics, vol. 36, no. 3, pp. 3028-3041, March 2021.

[29] W. Du, Q. Fu and H. F. Wang, "Power System Small-Signal Angular Stability Affected by Virtual Synchronous Generators," in IEEE Transactions on Power Systems, vol. 34, no. 4, pp. 3209-3219, July 2019.

Yaqian Yang received the Master degree in Electrical Engineering from the Changsha University of Science and Technology in 2018. and the Ph.D. degree in electrical engineering from Hunan University, Changsha, China, in 2022. She is currently an associate professor with the department of electrical engineering, Anhui Agricultural University, Hefei, China. Her current research interests include: stabilization and control of grid-forming virtual synchronous generators, synthetic inertial applied in hybrid AC/DC microgrids.

Chang Li obtained his bachelor degree in 2014 at Guizhou University, and obtained PhD degree in July 2020 at Hunan University. After his graduation of PhD career, he began his postdoc scientific work at Technical University of Denmark until October 2021. He was also a guest Senior Lecturer from September 2021 to December 2021 and from April 2022 to October 2022 at Peter the Great Saint Petersburg Polytechnic University. Since December 2021, he began his Postdoctoral Fellow career at Hong Kong Polytechnic University. Also, he was a Research Fellow at Nanyang Technological University since June 2022. He is currently an Associate Professor at Hefei University of Technology. His research interests are modeling, analysis and control of power electronics interfaced power systems.

Long Cheng received the M.S. degree in control engineering from Anhui University, Hefei, China, in 2015, and the Ph.D. degree in electrical engineering from Nanjing University of Aeronautics and Astronautics, Nanjing, China, in 2020. He is currently a lecturer with the department of electrical engineering, Anhui Agricultural University, Hefei, China. His research interests include power converters, energy storage technology, dc power supply system.

Xingle Gao received the B.Eng. degree in electrical engineering from North China University of Science and Technology, Tangshan, China, in 2015, and the M.Eng. degree in control science and engineering from Beijing University of Technology, Beijing, China, in 2018, and the Ph.D. degree in electrical engineering from Hunan University, Changsha, China, in 2022. He is currently an engineer with Economic Research Institute of State Grid Hebei Electric Power Co., Ltd, Shijiazhuang, China. His research interests include the modeling of electrical networks, and applications of complex networks in the assessment of robustness of power systems and cyber-physical systems.

Jiazhu Xu was born in Chuzhou, China, in 1980. He received the B.S., M.S., and Ph.D. degrees in electrical engineering from Hunan University, Changsha, China, in 2002, 2004, and 2007, respectively. Since 2008, he has been an Associate Professor with the College of Electrical and Information Engineering, Hunan University, where he became a Professor in 2017. His current research interests include AC/DC power conversion theory, locomotive traction power supply systems, and optimization of modern electrical equipment.

Frede Blaabjerg (S'86–M'88–SM'97–F'03) was with ABB-Scandia, Randers, Denmark, from 1987 to 1988. From 1988 to 1992, he got the PhD degree in Electrical Engineering at Aalborg University in 1995. He became an Assistant Professor in 1992, an Associate Professor in 1996, and a Full Professor of power electronics and drives in 1998. From 2017 he became a Villum Investigator. He is honoris causa at University Politehnica Timisoara (UPT), Romania and Tallinn Technical University (TTU) in Estonia.

His current research interests include power electronics and its applications such as in wind turbines, PV systems, reliability, harmonics and adjustable speed drives. He has published more than 600 journal papers in the fields of power electronics and its applications. He is the co-author of four monographs and editor of ten books in power electronics and its applications